Journal of Applied Fluid Mechanics, Vol. 17, No. 6, pp. 1191-1203, 2024.
Available online at www.jafmonline.net, ISSN 1735-3572, EISSN 1735-3645.
https://doi.org/10.47176/jafm.17.6.2369

Experimental and Numerical Investigation of Tip Leakage Vortex Cavitation in Water-jet Pump

Y. Long[1†], Z. Zhou[1], N. Li[2], M. Zhang[1], C. An[1], Y. Chen[1] and R. Zhu[1]

[1] *National Research Center of Pumps, Jiangsu University, Zhenjiang, Jiangsu, 212013, China*
[2] *Marine Design and Research Institute of China, Shanghai, 200011, China*

†*Corresponding Author Email: longyun@ujs.edu.cn*

ABSTRACT

During the operation of a water-jet pump, cavitation generates noise and vibration, causes surface erosion of the hydraulic components, and reduces the performance of the pump. Suppressing the cavitation is beneficial for improving the stability of the energy system of the water-jet pump. In order to investigate the mechanism of cavitation suppression and optimize the cavitation performance of the water-jet pump, the unsteady cavitation flow was studied by numerical simulation and experiment in this paper. Using high-speed photography technology on a closed test platform, the cavitation flow structures in the water-jet pump were captured, and the physical process of cavitation evolution was revealed. Based on this, in order to obtain the cavitation flow characteristics closely related to the cavitation performance, the cavitation flow in the impeller tip clearance was studied by numerical simulation, the vorticity variation rate in the tip clearance was analyzed, the effects of different cavitation conditions on the vorticity in the tip clearance were revealed. Additionally, this paper analyzed the pressure pulsation characteristics of the tip clearance under different cavitation conditions, and emphatically analyzed the influence of the cavitation flow on the tip clearance pressure pulsation.

Article History

Received October 10, 2023
Revised December 26, 2023
Accepted January 12, 2024
Available online March 27, 2024

Keywords:

Water-jet pump
Cavitation
Tip leakage vortex cavitation
Pressure pulsation
High speed photography

1. INTRODUCTION

Water-jet propulsion systems, commonly used in high-speed vessels, generate thrust by ejecting a jet of water backwards. At present, significant advancement has been achieved in studies of intake ducts (Huang et al., 2019). However, the design of water-jet pumps with high speed, high efficiency and high anti-cavitation performance is restricted by the requirements of structural dimensions and cavitation performance. Cavitation in the hydraulic components causes numerous adverse effects on the water-jet pumps, such as increasing vibration and noise, reducing thrust, and reducing efficiency. Long-term operation of water-jet pumps under cavitation conditions will cause the hydraulic components to erode. This will need serious suspension repair or component replacement for the hydraulic components with surface erosion, which will reduce energy delivery efficiency and increase maintenance costs. The deterioration in performance of water-jet pumps also affects the maneuverability of the vessel. Therefore, the study of tip leakage vortex cavitation in water-jet pumps can help optimize the impeller, improve cavitation performance and reduce vibration and noise while ensuring high efficiency.

Cavitation involves complex physical processes such as phase transition and unsteady vortices of vapor and liquid. The interaction of bubbles and liquid in cavitation flow causes complex two-phase turbulence, which involves the transfer of mass, momentum, and energy. The numerical method of cavitation faces a huge challenge in predicting and simulating cavitation vortex flow accurately. The numerical simulation of cavitation flow using suitable cavitation models has received more and more attention in recent years due to the advances in computational fluid dynamics (Li et al. 2021a; Yan et al., 2022; Kang et al., 2023; Li et al., 2023; Wang et al., 2023).

In 2018, Yan et al. (2018) analyzed the turbulence intensity, Reynolds stress and pressure pulsation of the suction surface of a water-jet pump with different blade profiles. It is found that the cavitation characteristics of the water-jet pump are closely related to the position of maximum blade thickness. The interrelation between the geometric structure of the blade and cavitation

characteristics is established. In 2019, Al-Obaidi et al. (2019) proposed a signal processing method based on envelope spectral analysis that effectively separates cavitation inception from the baseline. Li et al. (2019) reviewed the relevant experimental studies and new numerical methods on the transient characteristics and formation mechanisms of hydraulic machinery systems. Based on this, suggestions were made for the selection of simulation methods and further research directions. Yu et al. (2019) studied the hydrodynamic characteristics of different tip clearances of a water-jet pump. It is found that the dimension of the clearance does not change the fluctuation frequency of thrust and torque, but affects the fluctuation amplitude. In 2020, Han and Tan (2020) used the SST k-ω turbulence model to analyze the oscillating frequency of the tip leakage vortex of a mixed flow pump. It is found that the rotating speed and separation angle are positively correlated with the oscillation frequency. The author of this paper, Yun et al. (2020) proposed a new method to predict cavitation performance and verified its feasibility through experiment. Zhang et al. (2020a) investigated unsteady flow structures and pressure pulsations under off-design conditions using the DDES (Delayed Detached Eddy Simulation) method. In 2021, Zhao et al. (2021) investigated the evolution of cavitation in a water-jet pump under the influence of non-uniform inlet guide vanes wakes through cavitation experiment and numerical calculation. The research indicates that the non-uniform unsteady inflow is the primary cause of the uneven and intermittent of cavities. In 2022, Kang et al. (2022) analyzed the cavitation flow structures in a condensate pump and revealed the evolution process of cavitation during start-up. Wang et al. (2022) studied the influence of blade outlet angle on the internal flow characteristics of centrifugal pump under the cavitation condition, and determined the best blade outlet angle. Zhao et al. (2022) utilized an Zwart cavitation model combined with the DDES method to numerically simulate the cavitation flow in a water-jet pump. The study captured the cavitation patterns and the vortex development under both light and heavy cavitation conditions, analyzed the impact of cavitation on hydrodynamic load, and revealed the mechanisms of the evolution and interaction of wake vortices. The results indicate that the interaction between the thicken sheet cavitation and the diffuser wakes causes a shift in the dominant frequency of thrust load. In 2023, Chen et al. (2023) utilized an improved thermal cavitation model to investigate the impact of the tip leakage vortex, considering thermodynamic effects, on energy dissipation in a liquid nitrogen inducer.

To sum up, the current research concentrates on the mechanisms of cavitation unsteady flow and cavitation two-phase flow, but ignores the correlation between cavitation flow structures and pump performance. Aiming to propose a cavitation prediction method of the water-jet pump, the visualization experiment on the cavitation flow characteristics is conducted in this paper. Through further numerical simulation, the cavitation flow in the impeller tip clearance is studied, and the distribution of vorticity variation rate in the tip clearance of the impeller are analyzed.

2. CAVITATION TEST

2.1 Pump Comprehensive Performance Test Bench

A closed-type experimental loop is used to conduct the cavitation performance test. Figure 1 shows the real experimental system of the water-jet pump. The occurrence of cavitation can destroy the energy exchange in the pump, which is manifested in the external characteristics as a decrease on the flow-head curve, flow-efficiency curve, and flow-power curve. The active cavitation method is employed in this paper to induce cavitation in the pump, which involves vacuuming the suction tank to reduce the inlet pressure.

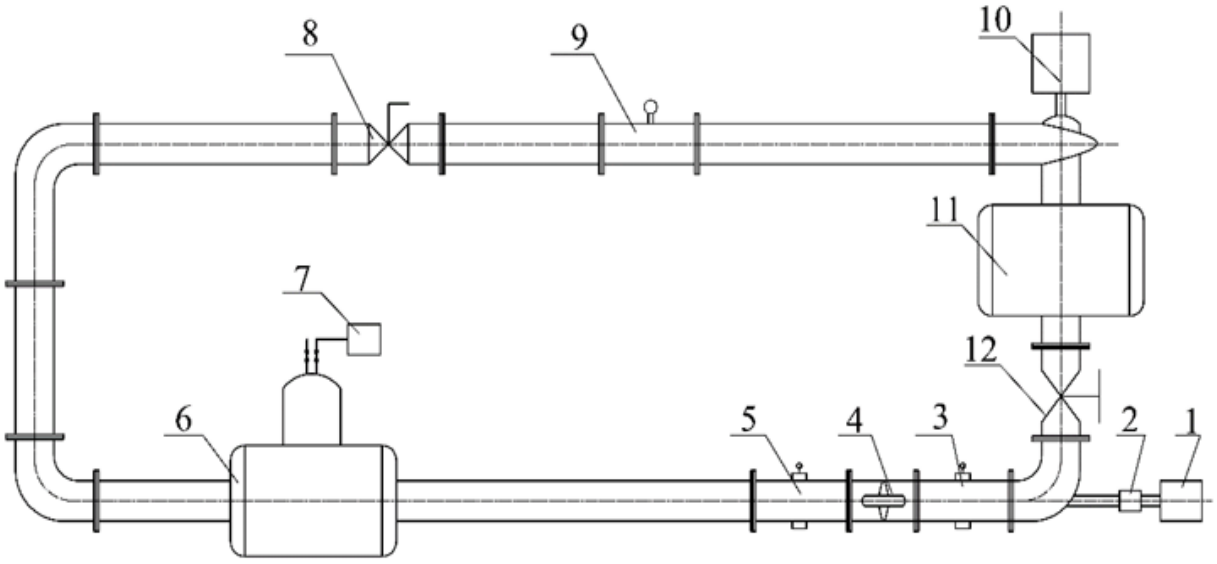

1.Motor 2. Torquemeter 3. Outlet pressuremeter 4. model pump 5. Inlet pressuremeter 6. Vacuum tank
7. Vacuum pump 8. Valve 9. Electromagnetic flowmeter 10. Booster pump 11. Buffer tank 12. Valve for adjusting

Fig. 1 Closed-circulation system of water-jet pump

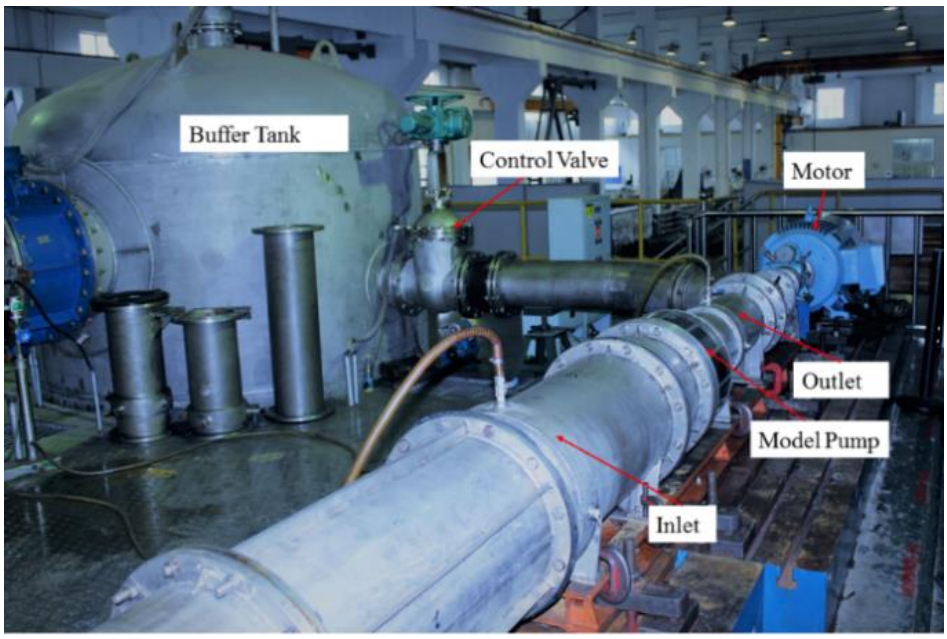

Fig. 2 Experimental system of water-jet pump

2.2 High Speed Photography Acquisition System

Theoretical methods can be used to preliminarily predict the internal flow state of fluid machinery and optimize its performance. However, it is quite difficult to achieve accurate prediction and design. Various methods are available to obtain internal flow characteristics in pumps. Some common measurement techniques for complex flow structures are Laser Doppler Velocimetry (LDV), Particle Image Velocimetry (PIV) and High-Speed Photograph (HSP). HSP technology can obtain not only the velocity distribution, but also the trajectory of fluid motion, and visually representation the evolution of fluid motion (Zhang et al. 2020b; Lu et al. 2022; Chang et al. 2023; Luo et al. 2023; Wu et al. 2023; Gong et al. 2023). It has been widely applied to visualize the morphology and development of cavitation flow in pumps.

A Plexiglas visual window is installed on the impeller shroud to visualize the cavitation flow pattern in the impeller. Figure 3 shows the structure diagram of high-speed photography experiment of the water-jet pump. The system consists of the high-speed camera, stroboscope and image information acquisition system. A high-speed camera PCO.dimax S1 is used, which ensures good image quality. It has high photosensitivity and dynamic range. To capture the cavitation evolution process completely, the sampling frequency is set to 4350 Hz, that is, to shoot an image every 2° rotation of the impeller. The camera lens is about 0.5 m away from the Plexiglas, and the area of the shooting region is 100 mm × 200 mm. So as to capture the cavitation evolution process completely, the sampling frequency of the high-speed camera is set to 4350 Hz, that is, to shoot an image every 2° rotation of the impeller.

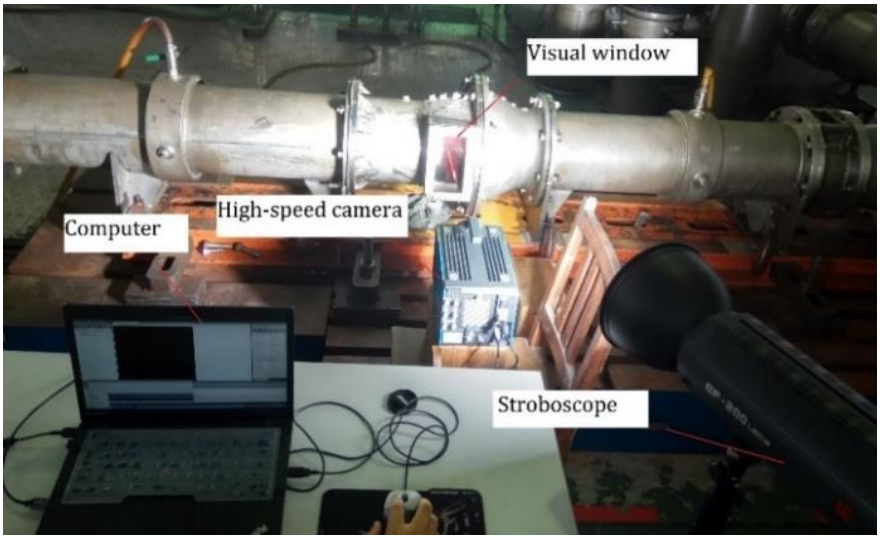

Fig. 3 High-speed photography visualization system

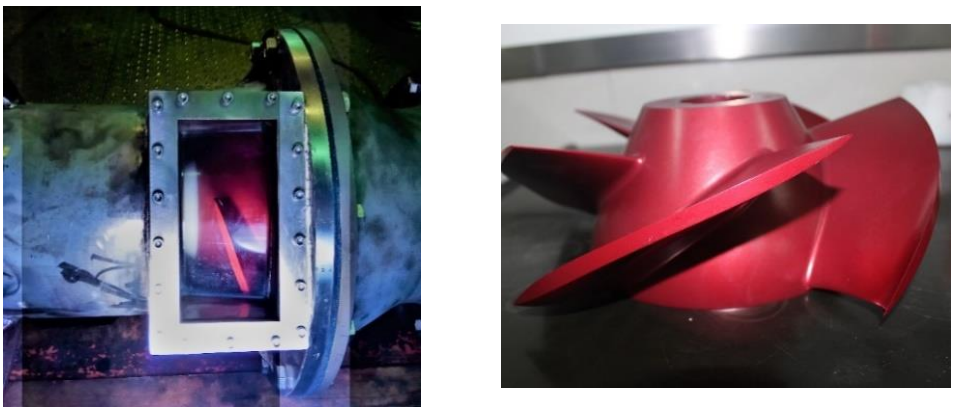

(a) Assembly (b) Impeller

Fig. 4 Real hydraulic components of water-jet pump

2.3 Water-jet Pump Model

The research object of this paper is a mixed-flow water-jet pump. Table 1 shows the main design parameters. The expression of specific speed n_s indicated in the table is as follows:

$$n_s = \frac{3.65n\sqrt{Q}}{H^{3/4}} \quad (1)$$

Where, n is the impeller rotating speed, r/min, Q is the volume flow, m^3/s, and H is the head, m. The entity of the water-jet pump and the impeller are shown in Fig. 4. Figure 5 shows the geometric model. The different cavitation states are obtained by adjusting the parameters of the device. In the process of adjusting the parameters of the device, the high-speed camera captures the images through the Plexiglas window installed on the impeller shroud.

Table 1 Design parameters of test pump

Design Parameters	Design value
Flow Q (m^3/s)	0.46
Head H (m)	13
Rotating speed n (r/min)	1450
Power P (kW)	70
Specific speed n_s	524.3
Impeller inlet diameter D_j (mm)	270

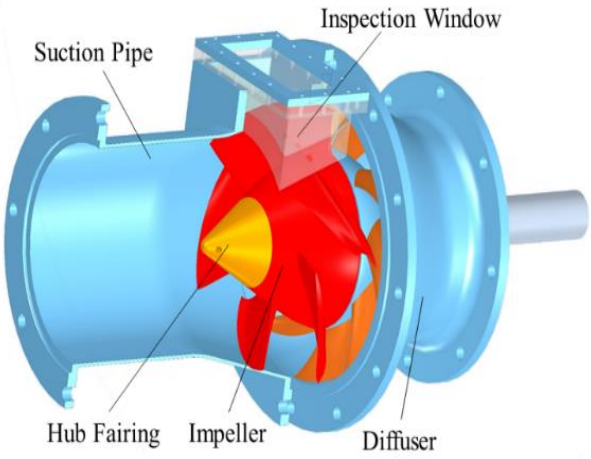

Fig. 5 Geometric model of water-jet pump

3. NUMERICAL CALCULATIONS

3.1 Meshing

The structural grids are utilized for the whole calculation domain. The calculation domains of the suction and the outpipe are meshed by the meshing software ICEM CFD. The geometric models of the impeller and diffuser are created with the turbomachinery blade design software BladeGen. The blade is created with 5 spans. The spline curve is used to fit the profile of each span of the blade. The leading edge and the trailing edge are elliptical. The domains of the impeller and diffuser are meshed with TurboGrid. The normal distance of the tip clearance is set to 0.3 mm. To precisely simulate the cavitation in the tip clearance, meshing of the tip clearance is critical. To better obtain the three-dimensional flow structures, the tip clearance domain is meshed with 25 layers of grids. For the grid independence verification, the geometric dimensions and the operating condition of the calculation model studied in the paper are similar to the water-jet pump model of Huang et al. (2015). According to the grid independence verification in Huang et al.'s study, to enhance the calculation accuracy, the grids of the impeller should be more than 1.06 million. The total grid number is about 4.13 million. The grid numbers of the calculation domains of the suction, impeller, diffuser and outpipe are 0.45 million, 1.27 million, 2.04 million and 0.37 million respectively. Figure 6 shows the grids of the computational domain for each hydraulic component.

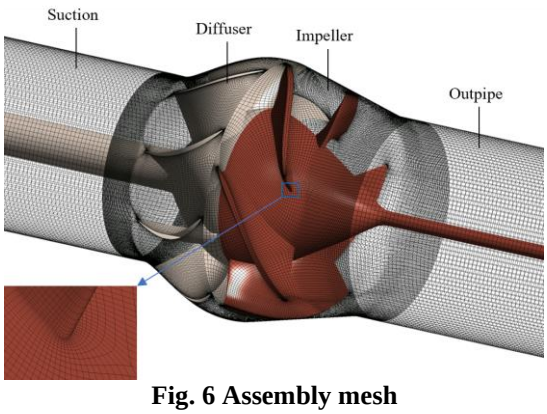

Fig. 6 Assembly mesh

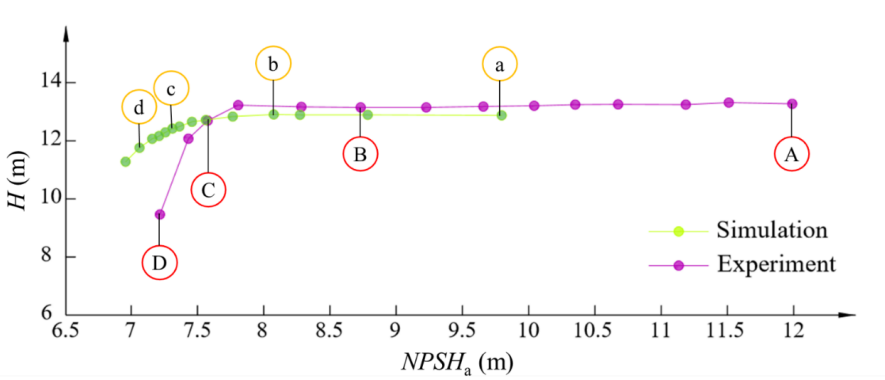

Fig. 7 Cavitation flow structure numerical calculation and experimental comparison conditions

3.2 Numerical Setting

The CFD software CFX is employed to simulate the unsteady cavitation flow in the water-jet pump. Water and water vapor at a temperature of 25°C are selected as the flow medium, with the corresponding physical properties: the density of water is 998 kg/m^3; the dynamic viscosity of water is 1.139×10^{-3} Pa·s; the saturated vapor pressure of water at 25°C is 3574 Pa; the density of water vapor is 0.02308 kg/m^3; the dynamic viscosity of water vapor is 9.8626×10^{-6} Pa·s. In this paper, the SST *k-ω* model with high precision is selected as the turbulence model. Considering the wide application of the Zwart–Gerber–Belamri (ZGB) model in the cavitation prediction in pumps, ZGB model is chosen as the cavitation model (Li et al. 2021b; Huan et al. 2021). The suction, diffuser, and outpipe are set to Stationary. The impeller is set to Rotating, and the angular velocity is 1450 r/min. The Wall Velocity of the impeller shroud is set to Counter Rotating Wall. The inlet boundary condition is pressure inlet. The outlet boundary condition is mass outlet. The wall boundary condition is set to No Slip Wall. The interface of dynamic and static calculation domain is set to Frozen Rotor Interface. The computational convergence accuracy is defined as 10^{-5}.

4. Analysis of Results

4.1 Cavitation Development Process

The cavitation performance curves of the water-jet pump, obtained from simulation and experiment under design conditions, are presented in Fig. 7. The points A–D on the experimental cavitation performance curve represented the different cavitation conditions correspond to the points a–d on the simulated cavitation performance curve. By comparison, it is found that the relative error between the rated head and the head obtained from numerical calculation of the model pump is about 3.5%. This demonstrates the reliability of the numerical simulation. The inlet pressure is reduced until cavitation occurring with the constant flow rate. Net Positive Suction Head Available ($HPSH_a$) is a parameter used to assess the likelihood of cavitation occurring in a pump. $NPSH_a$ indicates the amount of head that exceeds the vapor pressure of the fluid at the inlet of a pump. The expression for $NPSH_a$ is as follows:

$$HPSH_a = \frac{p_s}{\rho g} + \frac{v_s^2}{2g} - \frac{p_v}{pg} \tag{2}$$

When the experimental head decreases by 3%, $NPSH_a$ is 7.58 m, whereas corresponding simulated $NPSH_a$ is 7.15 m. This difference might result from neglecting non-condensable gases, thermodynamical effects, and other factors. However, it does not prevent the numerical calculation of cavitation flow structures in the water-jet pump. When $NPSH_a$ is larger, there is no cavitation in the pump. The energy characteristics of the pump are not affected, and the head remains unchanged. The point A on the experimental cavitation performance curve is regarded as the Non-Cavitation Condition. Although cavitation is generally considered absent, the cavitation of the tip of the blade can be observed from visual observation, which does not affect the performance. The point B at the experimental cavitation performance curve is the point where the flow-head curve begins to change. The head begins to increase at this point and then decreases. Additionally, in the visualization experiment, significant cavitation phenomenon occurs in the pump under this operating condition. Therefore, the point B is defined as the Inception Cavitation Condition. As the inlet pressure continues to decline, the head slightly increases before sharply dropping. The point C defined as the Critical Cavitation Condition corresponds to a 3% head reduction. Further reduction of the inlet pressure can result in a serious deterioration of the performance, leading to the occurrence of the Breakdown Cavitation Condition corresponding to the point D.

Figure 8 shows the cavitation flow structures captured by the visualization experiment. The different cavitation stages correspond to the points A-D in Fig.7. The cavities production increases gradually with the decrease of $NPSH_a$. The cavitation flow structures at the Non-Cavitation Condition are shown in Fig. 8 (a). Although there is no fluctuation of the performance curve in Fig. 7, the tip vortex cavitation can be observed. It is evident that bubbles are not formed on the pressure surface. The tip leakage vortex cavitation sheds on the front of the suction surface. There are a large number of shedding vortex filaments. In the middle region of the flow passage, the tip leakage vortex cavitation collapses completely in the middle region of the flow passage. Bubbles are not observed in the rear region of the flow passage, with little effect on the pressure side of the

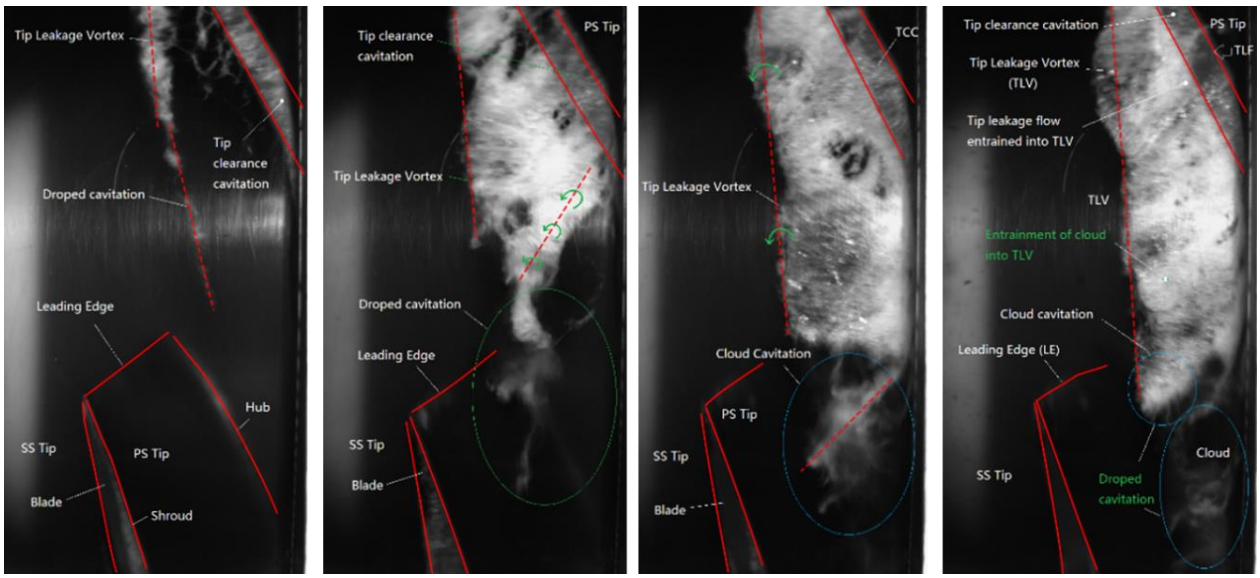

(a) Point A (b) Point B (c) Point C (d) Point D

Fig. 8 Cavitation flow structures at different cavitation development

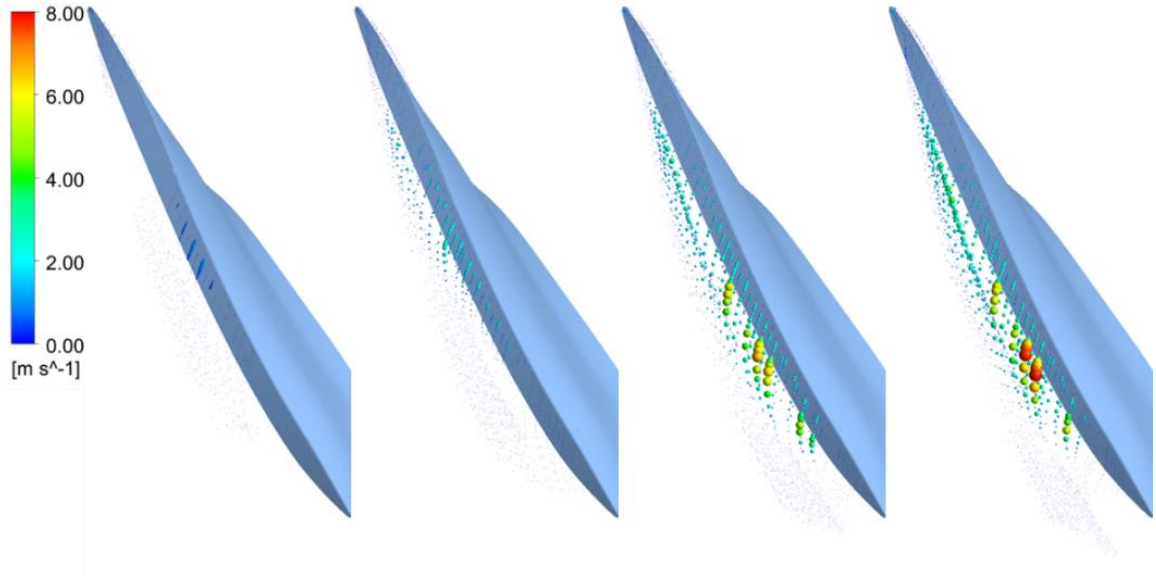

(a) Point a (b) Point b (c) Point c (d) Point d

Fig. 9 Velocity of vapor in tip clearance of impeller

adjacent blade. In Fig. 8 (b), the cavitation at the point B is more intense than at the point A. A triangular cloud cavitation structure can be observed in the flow passage. The triangular cloud cavitation is mainly affected by the entrainment effect of the tip leakage vortex, the tip leakage flow and the main flow. At the rear of the triangular region, the shedding bubbles collapse during the movement. The shedding cavitation vortex oscillates continuously. There is no definite low-pressure center of the vortex core. The adverse pressure gradient causes the vortex breakdown, resulting in the disappearance of the vortex core. Figure 8 (c) shows the cavitation state at the point C. Both the number and volume of bubbles increase in the tip leakage vortex at the point C. The region of cavitation extends towards the direction of the main flow. The entrainment of the tip leakage vortex becomes more intense. Referring to Fig. 8 (d), the cavitation shedding from the suction surface extends to the pressure side of the adjacent blade, causing serious blockage of the flow passage. At this time, the blade tip is covered by a large number of bubbles. This process promotes and induces the initiation and growth of cavitation on the adjacent blade, causing a sharp decline in head.

To observe the tip leakage vortex cavitation more clearly, as shown in Fig. 9, the velocity of vapor in the tip clearance under different cavitation stages is obtained. Compared with Fig. 8, the test results at each cavitation stage are consistent with the numerical simulation results. At the point a, the cavitation occurs in the tip clearance, resulting in the distribution of low velocity vapor. Under the effect of impeller rotation, the bubbles in the tip

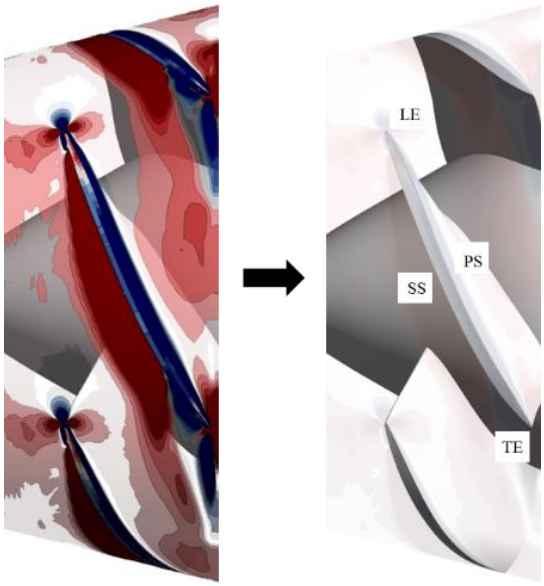

Fig. 10 Contour diagram with transparence

clearance spread on the suction surface and move towards the main flow direction. With the development of cavitation, it can be seen that the range of tip leakage vortex cavitation gradually expands. Besides, with the intensification of cavitation, the vapor velocity is also increasing and reached the highest in the Breakdown Cavitation Condition. Compared with Fig. 9 (c) and (d), after reaching the Critical Cavitation Condition, there is no obvious change in the distribution of the bubbles in the tip clearance. In order to conduct a more in-depth analysis of the tip clearance vortex, the section with r/R=99.9% is selected, and the vorticity analysis is performed in the tip clearance.

4.2 Vorticity Analysis

The influence of cavitation on the vortex structures in the tip clearance is analyzed using the vorticity transport equation. Based on the Navier-Stokes equations, The Z-axis component of the vorticity transport equation is as follows (Gopalan & Katz, 2000):

$$\frac{D\vec{\omega}_Z}{Dt}=\left((\vec{\omega}\cdot\nabla)\vec{u}\right)_Z-\vec{\omega}_Z(\nabla\cdot\vec{u})+\left(\frac{\nabla\rho_m\times\nabla p}{\rho_m^2}\right)_Z+(v_m+v_t)\nabla^2\vec{\omega}_Z \quad (3)$$

On the left side of Eq. (3), $\frac{D\vec{\omega}}{Dt}$ is the vorticity variation rate. On the right side of Eq. (3), $(\vec{\omega}\cdot\nabla)\vec{u}$ is the vortex stretching term, $-\vec{\omega}(\nabla\cdot\vec{u})$ is the vortex dilatation term, $\frac{\nabla\rho_m\times\nabla p}{\rho_m^2}$ is the barotropic torque term, and $(v_m+v_t)\nabla^2\vec{\omega}$ is the viscous diffusion term. The Reynolds number is large, with an order of magnitude of about 10^6 near the blade tip. The viscous diffusion term is relatively too small to be usually ignored.

In order to illustrate the position of the impeller blade in the contour diagram of the vorticity variation rate, a transparent diagram is provided as shown in Fig. 10, taking the point D which is the Breakdown Cavitation Condition, as an example. In the tip clearance, the interface between the positive and negative regions with larger area is mainly located at the SS. Due to the existence of the cavitation region, the outflow phenomenon occurs at the position of the blade near the TE. Therefore, at the position close to the TE, the interface between the two regions is not bounded by the SS plane. The evolution of this boundary with the increase of cavitation will be analyzed in Fig. 11. The contours of the vorticity variation rate and each term in the Z direction on the spanwise section in the tip clearance (r/R=99.9%) under different cavitation conditions are shown in Fig. 11-13.

For the distribution of vorticity variation rate in the Z direction shown in Fig. 11, the larger absolute value of vorticity in each condition is mainly distributed at the LE, the SS and the tip clearance. At all the conditions, the absolute value of the relatively large vorticity

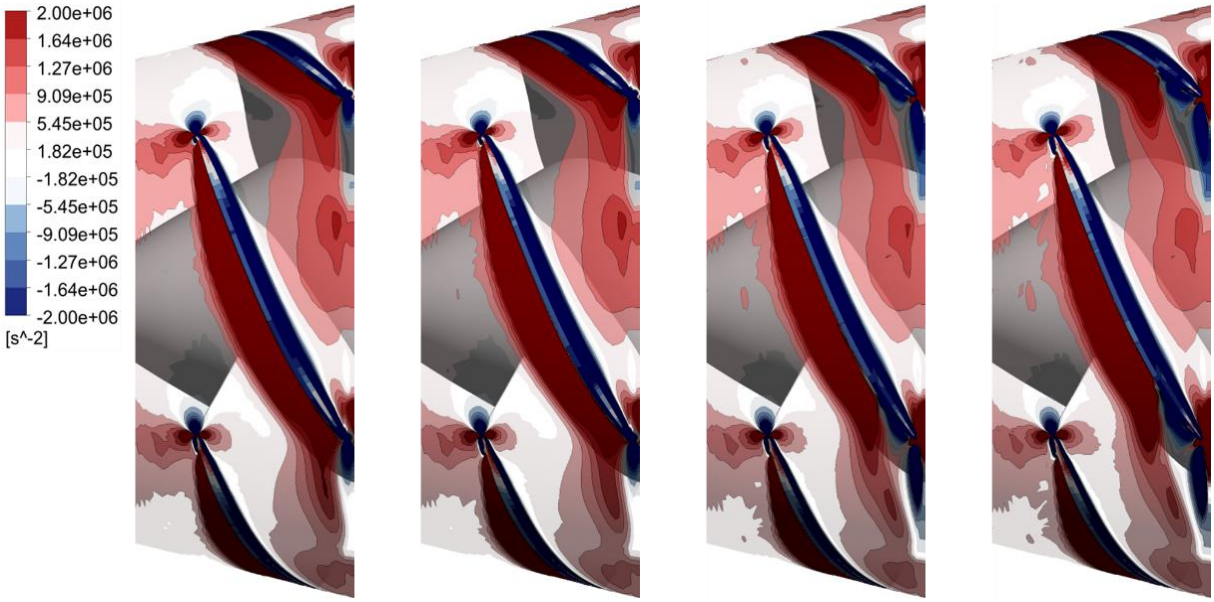

(a) Point a (b) Point b (c) Point c (d) Point d

Fig. 11 Contours of vorticity variation rate on spanwise section at r/R=99.9%

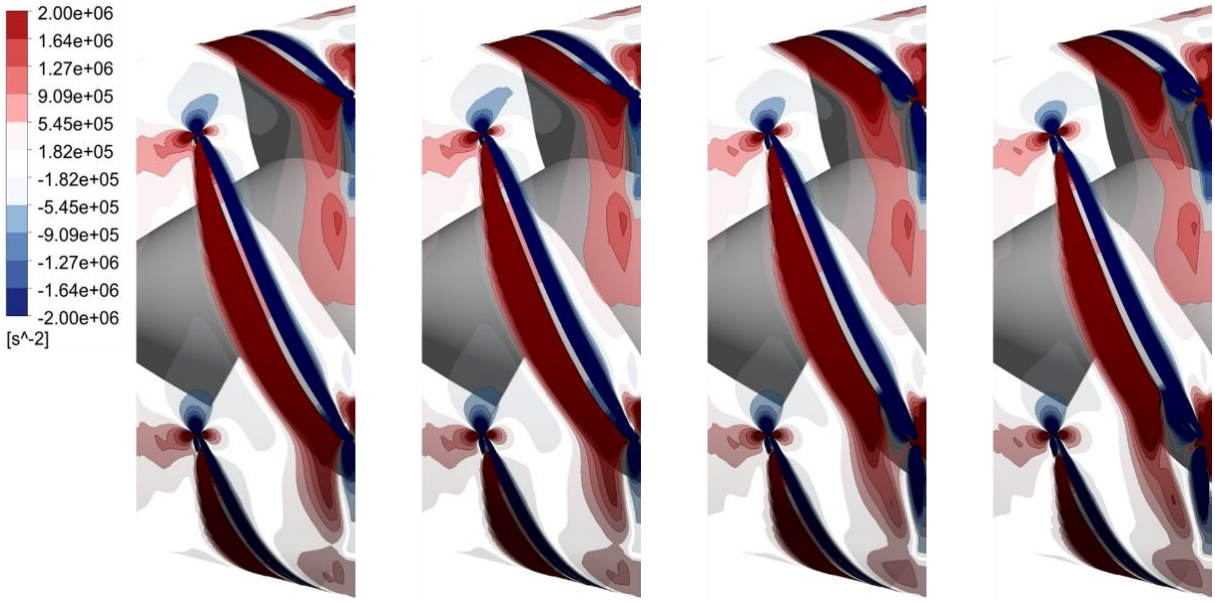

(a) Point a (b) Point b (c) Point c (d) Point d

Fig. 12 Contours of vortex stretching term on spanwise section at *r*/*R*=99.9%

distributed near the LE and the tip clearance is unchanged. This is attributed to two factors: Firstly, the cavitation does not appear at the LE during the development of cavitation. Secondly, as can be observed from Fig. 9, there is minimal difference in the cavitation in the tip clearance under different conditions. The difference of the vorticity distribution at the SS is mainly near the TE. There is no significant difference in the vorticity distribution between Point A and Point B. However, starting from Point c, the positive vorticity region with larger absolute value begins to shed from the TE, while the area of the negative vorticity region with a relatively large absolute value begins to increase. In order to further explore the distribution of vorticity variation rate, vortex stretching term and vortex dilatation term are analyzed separately. In addition, the barotropic torque term is not obvious, so this analysis is ignored in this paper.

Figure 12 shows the distribution of the vortex stretching term in the tip clearance. The vortex stretching represents the change in the magnitude and direction of vorticity caused by the transformation of velocity gradient of flow field. There is little difference between the contour diagrams in Fig. 11 and Fig. 12, indicating that the vortex stretching plays a dominant role in each cavitation condition. At the LE near the incoming flow, due to the impact of the incoming flow at the LE, a region with a larger absolute value of the vortex stretching term is formed. Since there is no cavitation region, the vortex stretching term here is consistent under each cavitation condition. On the side close to the PS in the tip clearance, the vortex stretching can be observed as a negative value, indicating that the local vorticity here is caused by the pressure generated by the impeller rotation. On the SS, the vortex stretching is positive, indicating that the vortex on the SS is expanding. Near TE, the region where the vortex stretching term is negative expands with the aggravation of cavitation. This is because the backflow of the SS near the TE gradually increases caused by the expansion of the cavitation region, and reaches the maximum value during the Breakdown Cavitation Condition. Simultaneously, the area of the negative vortex stretching term region expands, causing the area of the positive vortex stretching term area to spread into the flow passage.

Further, Fig. 13 shows the distribution of the vortex dilatation term in the tip clearance. The vortex dilatation term is caused by the expansion and contraction of the fluid medium, which shows the effect of fluid compressibility. On the side close to the PS in the tip clearance, it can be observed that the vortex dilatation term is negative, and the fluid is in a compressed state. With the development of cavitation, at the TE near the incoming flow, the area of the positive vortex dilatation term region gradually decreases. This phenomenon is caused by the expansion of the backflow region.

In summary, the most significant effect of vorticity in the tip clearance is the vortex stretching term caused by the relative movement between the blade tip and impeller shroud. Moreover, with the intensification of cavitation, the development of cavitation at the SS leads to significant changes in the distributions of the vortex stretching term and the vortex dilatation term near the TE.

4.3 Pressure Pulsation

In this paper, the pressure pulsation in the tip clearance is analyzed in order to further explore the flow characteristics in the tip clearance. The monitoring points are set as shown in Fig. 14. Before the transient calculation, for the interface of dynamic and static calculation domain, the Frozen Rotor Interface set in the steady calculation is reset to Transient Rotor-Stator. The time step is set to 5.74713E-5 s, which is the time for the impeller to rotate by 0.5°. In the numerical simulation, 8

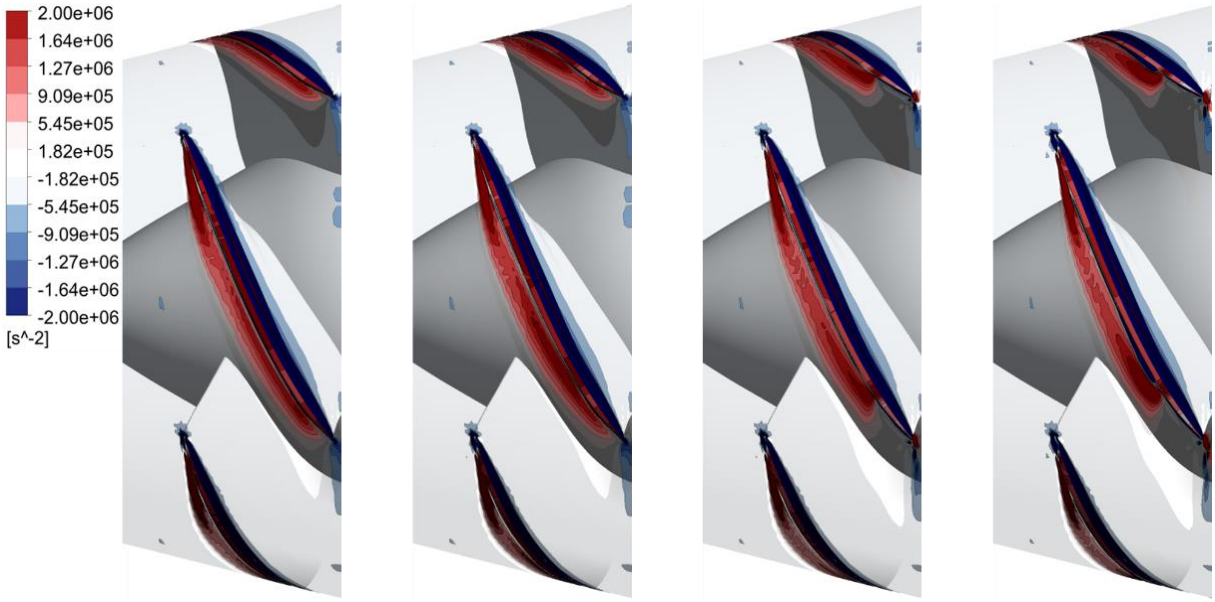

(a) Point a (b) Point b (c) Point c (d) Point d

Fig. 13 Contours of vortex dilatation term on spanwise section at *r*/*R*=99.9%

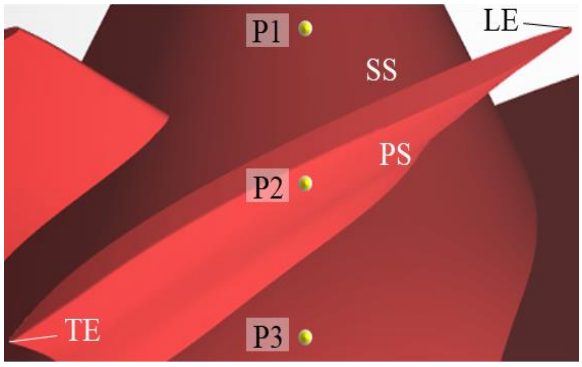

Fig. 14 Schematic diagram of monitoring points in tip clearance

impeller rotation cycles are calculated for each operating condition, and the data from the 8th cycle is used for analysis. The commercial software Origin is used to perform FFT (Fast Fourier Transform) on each group of data to obtain the frequency domain diagram of pressure pulsation at each monitoring point, as shown in Fig. 15-17.

As shown in Fig. 15, it is the spectrum diagram of pressure pulsation at P1. It shows that under the different cavitation stages, the main frequency of P1 is 217.5 Hz, which is the diffuser blade passing frequency (f_{DPF}). The diffuser blade passing frequency is 9 times of the impeller blade rotating frequency (f_R), and this multiple corresponds to the number of diffuser blades. At Point a

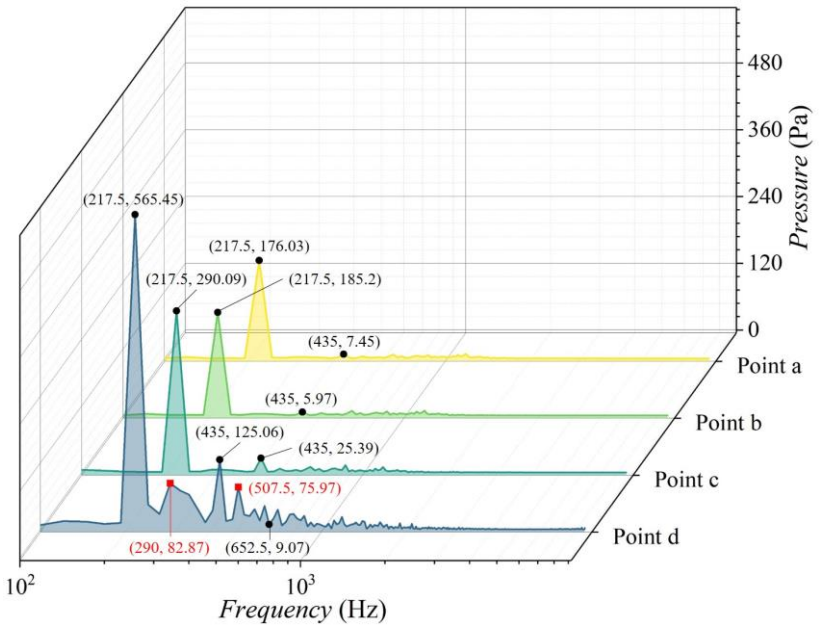

Fig. 15 Frequency domain diagram of pressure pulsation at point P1

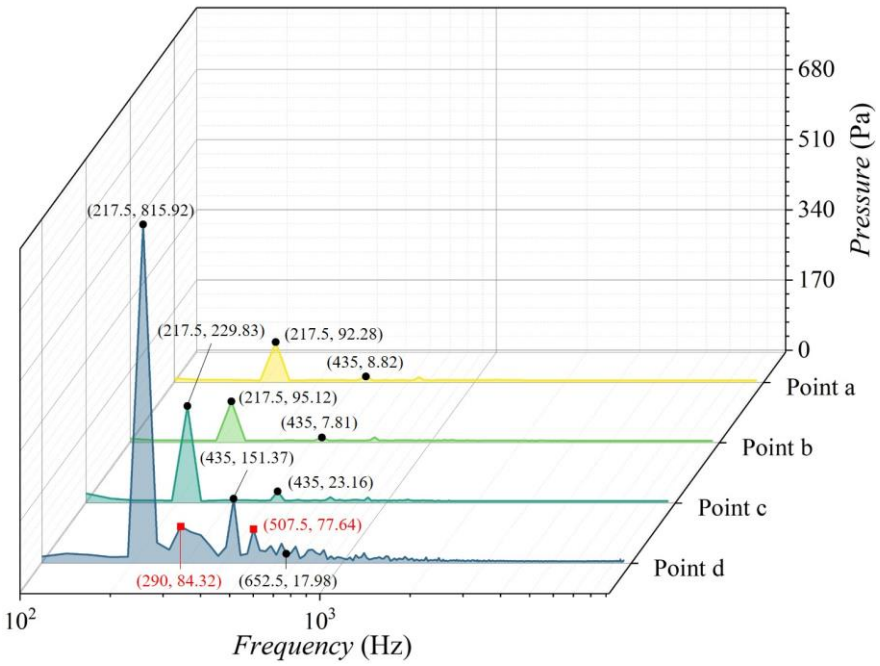

Fig. 16 Frequency domain diagram of pressure pulsation at point P2

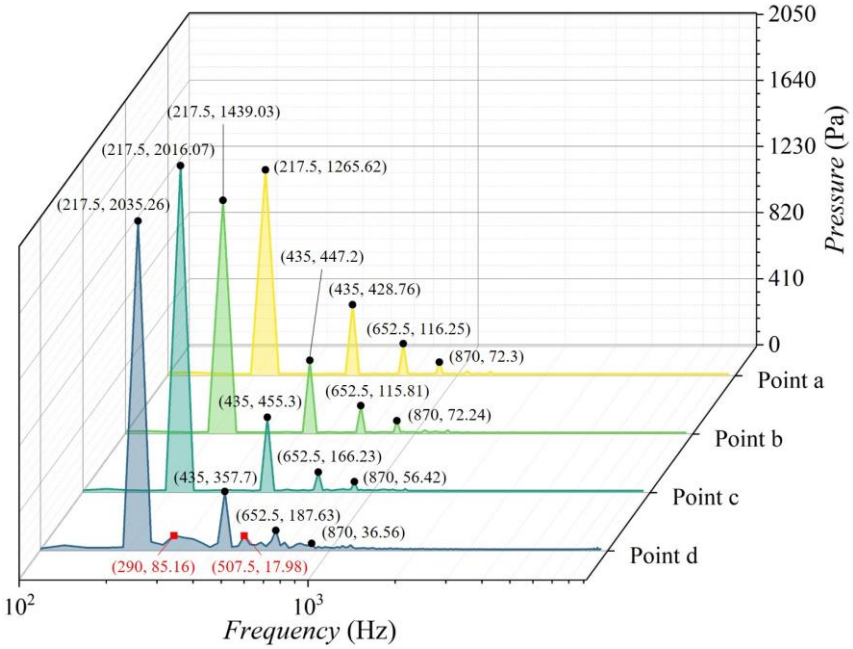

Fig. 17 Frequency domain diagram of pressure pulsation at point P3

and Point b, the amplitudes corresponding to f_{DPF} are relatively close. There is no significant amplitude appearing when the frequency is greater than f_{DPF}. With the intensification of cavitation, at Point c, the amplitude corresponding to $2f_{DPF}$ is more significant. Compared to Point b, the amplitude corresponding to f_{DPF} increases by 56.64%. At Point d, the amplitude corresponding to f_{DPF} reaches the maximum value, and the amplitude corresponding to $2f_{DPF}$ is 3.93 times higher than at Point c. The difference from the previous condition is that, at a frequency of 290 Hz (corresponding to $12f_R$) after f_{DPF}, there is an amplitude of 82.87 Pa. After $2f_{DPF}$, there is a larger amplitude corresponding to a frequency of 507.5 Hz, i.e. $21f_R$. An interesting phenomenon is that the amplitude corresponding to the frequency of $3f_{DPF}$ is smaller compared to the amplitude of adjacent frequencies. It can be seen that, under the Breakdown Cavitation Condition, despite the dominance of dynamic and static interference in the pressure pulsation, the influence of cavitation cannot be ignored. At the same time, the amplitude corresponding to f_{DPF} keeps increasing as cavitation intensifies.

The overall trend of pressure pulsation shown in Fig. 16 is similar to that of Fig. 15. Regarding Points a–c, the amplitude corresponding to f_{DPF} for each condition at P2 is smaller than that at P1. However, at Point d, the amplitude of f_{DPF} corresponding to P2 is 815.92 Pa, significantly higher than the amplitude of 565.45 Pa corresponding to P1. Comparing with Fig. 9, it is evident that the cavitation is significantly more intense at P2 than

at P1, further highlighting the promoting effect of cavitation on f_{DPF}.

The position of P3 is close to the TE in the tip clearance and is the closest position to the diffuser among all monitoring points. As shown in Fig. 17, the amplitude corresponding to f_{DPF} under each condition is much larger than that at P1 and P2. For Points a–c, the obvious amplitude at $2f_{DPF}$ - $4f_{DPF}$ can also be observed. For f_{DPF}, as cavitation develops from the Inception Cavitation Condition to the Critical Cavitation Condition, its amplitude significantly increases by 40.16%. When cavitation develops to the Breakdown Cavitation Condition, its amplitude does not change significantly. For $2f_{DPF}$, its amplitude slowly increases with the development of cavitation until the Critical Cavitation Condition. Its amplitude appeared to drop more obviously when it reached the Breakdown Cavitation Condition. Aiming at the frequency of 290 Hz with large amplitude during the Breakdown Cavitation Condition, there is no significant change in the amplitude of different monitoring points in the tip clearance. The pressure pulsation at P3 is more evident compared to P1 and P2, due to the dynamic and static interference between the impeller and the diffuser. The influence of cavitation has little effect on pressure pulsation relatively.

5. DISCUSSION

During the analysis of pressure pulsation, a higher amplitude is observed at each monitoring point in the tip clearance at a frequency of 290 Hz ($12f_R$) under the Breakdown Cavitation Condition. By comparing the amplitudes corresponding to $12f_R$ at the same location under different cavitation conditions, it can be concluded that the fluctuation amplitude only increases significantly when the Breakdown Cavitation Condition is reached. In other words, its relationship with the degree of cavitation is extremely close. However, it is interesting that although they are not at the same position, their corresponding amplitudes do not change much. The amplitudes at P1–P3 are 82.87 Pa, 84.32 Pa, and 85.16 Pa, respectively. At the same time, after $12f_R$, the amplitude still maintains a similar level until 14 f_R.

Regarding the above phenomenon, there are two main issues that need to be discussed: Firstly, the frequency corresponding to 290 Hz is $12f_R$, but this multiple does not have a significant relationship with the number of impeller blades or diffuser blades, so its source is still uncertain at present. Secondly, a sudden peak amplitude appears at $12f_R$ under the Breakdown Cavitation Condition, and the amplitude does not change significantly with the monitoring position. We will continue the research work on these two issues.

6. CONCLUSION

This paper presents an experimental and numerical study on the tip leakage vortex cavitation in a water-jet pump. The cavitation flow characteristics in the pump are captured through the visualization experiment. Furthermore, the cavitation and vorticity distribution in the tip clearance of the impeller are analyzed by numerical simulation. The primary findings and conclusions are as follows:

(1) Under the action of impeller rotation, the cavitation in the tip clearance spreads towards the suction surface and flows downstream with the fluid. As the cavitation intensifies, the region of tip leakage vortex cavitation gradually expands, and the vapor velocity also gradually increases, reaching its maximum value under the Breakdown Cavitation Condition.

(2) The most significant effect on vorticity in the tip clearance is the vortex stretching term caused by the relative movement between blade tip and shroud. At the same time, with the aggravation of cavitation, the development of the cavitation region at the SS causes the distribution of the vortex stretching term and the vortex dilatation term to change significantly.

(3) Before the Inception Cavitation Condition, the pressure pulsation in the tip clearance of the water-jet pump is mainly affected by the dynamic and static interference between impeller and diffuser. When reaching the Breakdown Cavitation Condition, although the main influence on the pressure pulsation is still dynamic and static interference, the impact of cavitation should not be ignored, and the intensification of cavitation can increase the fluctuation amplitude of f_{DPF}.

ACKNOWLEDGEMENTS

This work was funded by the China Postdoctoral Science Foundation Funded Project (Grant No. 2019M651734, 2023M733355), Jiangsu University Youth Talent Development Program (2020), the Chunhui Program Cooperative Scientific Research Project of the Ministry of Education, Research Project of State Key Laboratory of Mechanical System and Vibration (Grant No. MSV202203), Natural Science Foundation of China (Grant No. 51906085, U20A20292), Jiangsu Province Innovation and Entrepreneurship Doctor Project (2019).

Thanks to Dr. Li Yajie for improving the English writing of this article.

CONFLICT OF INTEREST

The authors declare that there are no conflicts of interest.

AUTHORS CONTRIBUTION

Yun Long: Conceptualization, Methodology, Supervision, Visualization; **Zhen Zhou:** Data curation, Formal analysis, Writing – Original draft; **Mingyu Zhang:** Data Curation, Validation, Writing – Original draft; **Ce An:** Methodology, Visualization, Writing – review & editing; **Yong Chen:** Supervision, Writing – review & editing; **Rongsheng Zhu:** Supervision, Writing – review & editing.

REFERENCES

Al-Obaidi, A. R., & Towsyfyan, H. J. J. O. A. F. M. (2019). An experimental study on vibration signatures for detecting incipient cavitation in centrifugal pumps based on envelope spectrum analysis. *Journal of Applied Fluid Mechanics*, *12*(6), 2057-2067. https://doi.org/10.29252/JAFM.12.06.29901

Chang, L., Xu, Q., Yang, C., Su, X., Wang, H., & Guo, L. (2023). Experimental study on gas–liquid flow patterns and bubble size in a high-speed rotating impeller of a three-stage centrifugal pump. *Experimental Thermal and Fluid Science*, *145*, 110896. https://doi.org/10.1016/j.expthermflusci.2023.110896

Chen, Z., Yang, S., Li, X., Li, Y., & Li, L. (2023). Investigation on leakage vortex cavitation and corresponding enstrophy characteristics in a liquid nitrogen inducer. *Cryogenics*, *129*, 103606. https://doi.org/10.1016/j.cryogenics.2022.103606

Gong, B., Zhang, Z., Feng, C., Yin, J., Li, N., & Wang, D. (2023). Experimental investigation of characteristics of tip leakage vortex cavitation-induced vibration of a pump. *Annals of Nuclear Energy*, *192*, 109935. https://doi.org/10.1016/j.anucene.2023.109935

Gopalan, S., & Katz, J. (2000). Flow structure and modeling issues in the closure region of attached cavitation. *Physics of fluids*, *12*(4), 895-911. https://doi.org/10.1063/1.870344

Han, Y., & Tan, L. (2020). Influence of rotating speed on tip leakage vortex in a mixed flow pump as turbine at pump mode. *Renewable Energy*, *162*, 144-150. https://doi.org/10.1016/j.renene.2020.08.033

Huan, Y. Y., Liu, Y. Y., Li, X. J., Zhu, Z. C., Qu, J. T., Zhe, L., & Han, A. D. (2021). Experimental and numerical investigations of cavitation evolution in a high-speed centrifugal pump with inducer. *Journal of Hydrodynamics*, *33*(1), 140-149. https://doi.org/10.1007/s42241-021-0006-z

Huang, R., Dai, Y., Luo, X., Wang, Y., & Huang, C. (2019). Multi-objective optimization of the flush-type intake duct for a waterjet propulsion system. *Ocean Engineering*, *187*, 106172. https://doi.org/10.1016/j.oceaneng.2019.106172

Huang, R., Ji, B., Luo, X., Zhai, Z., & Zhou, J. (2015). Numerical investigation of cavitation-vortex interaction in a mixed-flow waterjet pump. *Journal of Mechanical Science and Technology*, *29*, 3707-3716. https://doi.org/10.1007/s12206-015-0816-4

Kang, C., Lu, C., Seah, K. G., & Zhang, W. (2022). Cavitation characteristics during startup process of a condensate pump with splitter blades. *Journal of Applied Fluid Mechanics*, *15*(4), 1099-1109. https://doi.org/10.47176/JAFM.15.04.1082

Kang, W., Zhou, L., & Wang, Z. (2023). Analysis of flow characteristics and cavitation in the vanes of a reversible pump-turbine in pump mode. *Journal of Energy Storage*, *68*, 107690. https://doi.org/10.1016/j.est.2023.107690

Li, D., Fu, X., Zuo, Z., Wang, H., Li, Z., Liu, S., & Wei, X. (2019). Investigation methods for analysis of transient phenomena concerning design and operation of hydraulic-machine systems—A review. *Renewable and Sustainable Energy Reviews*, *101*, 26-46. https://doi.org/10.1016/j.rser.2018.10.023

Li, L. M., Wang, Z. D., Li, X. J., Wang, Y. P., & Zhu, Z. C. (2021a). Very large eddy simulation of cavitation from inception to sheet/cloud regimes by a multiscale model. *China Ocean Engineering*, *35*, 361-371. https://doi.org/10.1007/s13344-021-0033-0

Li, W., Liu, M., Ji, L., Li, S., Song, R., Wang, C., ... & Agarwal, R. K. (2023). Study on the trajectory of tip leakage vortex and energy characteristics of mixed-flow pump under cavitation conditions. *Ocean Engineering*, *267*, 113225. https://doi.org/10.1016/j.oceaneng.2022.113225

Li, X., Liu, Y., Zhu, Z., Lin, P., & Li, L. (2021b). Boundary vorticity analysis and shedding dynamics of transient cavitation flow around a twisted hydrofoil. *Journal of Fluids Engineering*, *143*(7), 071501. https://doi.org/10.1115/1.4050135

Lu, Y., Tan, L., Han, Y., & Liu, M. (2022). Cavitation-vibration correlation of a mixed flow pump under steady state and fast start-up conditions by experiment. *Ocean Engineering*, *251*, 111158. https://doi.org/10.1016/j.oceaneng.2022.111158

Luo, X., Yan, S., Sun, S., Feng, J., Xie, H., Zhang, L., & He, D. (2023). Experimental study of gas–liquid two-phase operating characteristics and bubble evolution law of a semi-open mixed-flow pump. *Ocean Engineering*, *272*, 113733. https://doi.org/10.1016/j.oceaneng.2023.113733

Wang, C., Guo, L., Liu, Z., Zhang, Y., & Li, Z. (2023). Unsteady flow analysis regarding stall flow and rotating cavitation in the first-stage of a multistage LNG cryogenic submerged pump. *Cryogenics*, *129*, 103546. https://doi.org/10.1016/j.cryogenics.2022.103546

Wang, Y. Y., Zhao, W. G., Han, H. D., Fan, P. J., Liu, Z. L., & Hu, J. Q. (2022). Effects of the centrifugal pump outlet blade angle on its internal flow field characteristics under cavitation condition. *Journal of Applied Fluid Mechanics*, *16*(2), 389-399. https://doi.org/10.47176/JAFM.16.02.1241

Wu, D., Ren, Y., Sørensen, H., Qian, H., & Mou, J. (2023). Gas-liquid flow patterns visualization in a self-priming centrifugal pump. *Flow Measurement and Instrumentation*, *92*, 102389. https://doi.org/10.1016/j.flowmeasinst.2023.102389

Yan, H., Li, Q., Zhang, Y., Shi, H. X., & Vnenkovskaia, V. (2018). Optimization of cavitating flow characteristics on RBSS of waterjet pumps.

International Journal of Simulation Modelling, *17*(2), 271-283. https://doi.org/10.2507/IJSIMM17(2)427

Yan, L., Gao, B., Ni, D., Zhang, N., & Zhou, W. (2022). Numerical analysis on the cavitation characteristics of a pump with an inducer in non-uniform inflow. *Ocean Engineering*, *256*, 111407. https://doi.org/10.1016/j.oceaneng.2022.111407

Yu, H., Zhang, Z., & Hua, H. (2019). Numerical investigation of tip clearance effects on propulsion performance and pressure fluctuation of a pump-jet propulsor. *Ocean Engineering*, *192*, 106500. https://doi.org/10.1016/j.oceaneng.2019.106500

Yun, L., Rongsheng, Z., & Dezhong, W. (2020). A cavitation performance prediction method for pumps PART1-Proposal and feasibility. *Nuclear Engineering and Technology*, *52*(11), 2471-2478. https://doi.org/10.1016/j.net.2020.04.007

Zhang, N., Jiang, J., Gao, B., & Liu, X. (2020a). DDES analysis of unsteady flow evolution and pressure pulsation at off-design condition of a centrifugal pump. *Renewable Energy*, *153*, 193-204. https://doi.org/10.1016/j.renene.2020.02.015

Zhang, W., Zhu, B., & Yu, Z. (2020b). Characteristics of bubble motion and distribution in a multiphase rotodynamic pump. *Journal of Petroleum Science and Engineering*, *193*, 107435. https://doi.org/10.1016/j.petrol.2020.107435

Zhao, G., Liang, N., Zhang, Y., Cao, L., & Wu, D. (2021). Dynamic behaviors of blade cavitation in a water jet pump with inlet guide vanes: Effects of inflow non-uniformity and unsteadiness. *Applied Ocean Research*, *117*, 102889. https://doi.org/10.1016/j.apor.2021.102889

Zhao, X., Shen, X., Geng, L., Zhang, D., & van Esch, B. B. (2022). Effects of cavitation on the hydrodynamic loading and wake vortex evolution of a pre-swirl pump-jet propulsor. *Ocean Engineering*, *266*, 113069. https://doi.org/10.1016/j.oceaneng.2022.113069